# ACMap: Across-scales Connectivity Mapping of Primate Brain

Runjia Lin[1,2][0009−0004−2115−2852], Tianjia Zhu[1,2][0009−0001−4601−6062], Minhui Ouyang[1,3][0000−0001−8013−2553], and Hao Huang[1,3](✉)[0000−0002−9103−4382]

[1] Department of Radiology, Children's Hospital of Philadelphia, PA, United States
[2] Department of Bioengineering, University of Pennsylvania, PA, United States
[3] Department of Radiology, University of Pennsylvania, PA, United States
huangh6@chop.edu

**Abstract.** Brain connectivity emerges from multiple scales, from mesoscale axonal projections to macroscale white matter (WM) tract pathways. Virus tracing provides gold standard axonal projection at $\mu$m level but is restricted by limited virus injection locations and lack of streamlines. Diffusion MRI (dMRI) can cover brain-wide connectivity streamlines but cannot measure cellular level connections. Across-scales connectivity mapping including gold standard virus tracer injection, ex vivo ultra-high-resolution dMRI, and in vivo regular dMRI tractography offers a unique, complementary and possibly the only solution to elucidate the brain-wide mesoscale connectome, at the level of $\mu$m, 100 $\mu$m and 1000 $\mu$m respectively. However, this is hindered by the lack of advanced techniques to generate large-scale and high-throughput streamlines from virus tracing data and to bridge across-scales connectivity. To directly integrate connectivity across scales, we propose ACMap, a novel framework that reconstructs high-fidelity streamlines from virus tracing. ACMap leverages fast marching method (FMM) with a simple and interpretable speed function for continuous tracing of fiber pathways by casting streamline propagation as a front evolution process, where the interface advances progressively outward from the injection site. The proposed ACMap reconstructs high-fidelity and dense streamlines, enabling across-scales integration and validation of fiber pathways derived from dMRI and virus tracer data. Qualitative and quantitative assessments demonstrate that ACMap outperforms other competitive methods by a large margin. Further comparison between ACMap streamlines and dMRI tractography streamlines shows consistency of traced fibers. ACMap represents a significant step towards mapping across-scales connectivity of the brain, providing a new approach for accurate mapping of the brain-wide mesoscale connectome.

**Keywords:** Virus tracing · Diffusion MRI · Tractography · Microscopy · Connectivity and network analysis.

## 1 Introduction

Brain connectivity emerges from multiple scales, from mesoscale axonal projections to macroscale WM tract pathways. Traditionally, dMRI is a modality of

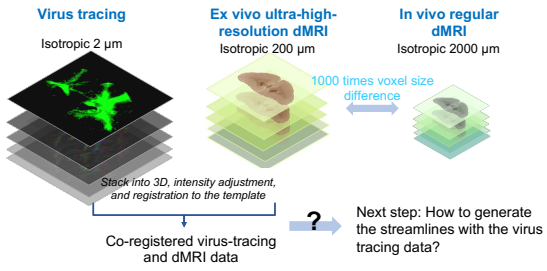


**Fig. 1. Integrating virus tracing and dMRI.** Virus tracing, ex vivo ultra-high-resolution dMRI, and in vivo conventional dMRI provide complementary insights into brain connectivity at resolutions of 2 $\mu$m, 200 $\mu$m, and 2000 $\mu$m, respectively. Ex vivo ultra-high-resolution dMRI has a voxel size 1000 times smaller than in vivo conventional dMRI. To integrate virus tracing with dMRI, virus tracing data is down-sampled and co-registered to ex vivo ultra-high-resolution dMRI. We aim to address the next step for generation of streamlines from virus tracing data and integration with dMRI tractography.

choice for noninvasively mapping brain connectome at macroscale. DMRI tractography with ultra-high-resolution brain dMRI is based on spatial resolutions of 10-100 micrometers [2, 5], while tractography with in vivo developmental brain dMRI is typically based on macroscopic spatial resolutions of 1,500-3,000 micrometers, e.g., [6, 4, 14]. However, limited by its highest possible spatial resolution of 10-100 micrometers, dMRI so far cannot directly measure cellular level connections.

Virus tracers genetically modify the proteins in neurons to make them fluorescent, thereby enabling microscopy imaging at cellular resolutions (micrometers or less). Although no method is an "absolute" gold standard for tracing axonal pathways, virus tracing is widely regarded as one of the closest experimental proxies for axonal connectivity, e.g. [1, 13], with its validity endorsed by the general basic neuroscientific field [23, 9]. Virus tracing with both anterograde and retrograde tracers offers a robust method for probing cellular level connectivity and validating dMRI tractography [1, 7, 8, 11, 13]. However, virus tracing experiments are invasive and costly, and each injection produces local axonal information instead of whole brain. While prior work has progressed neuron reconstruction from volumetric neuronal intensities [10, 20, 3, 24, 12, 27], they either primarily target single-neuron or sparsely labeled reconstructions [3, 24], rely on additional shape priors and thresholding assumptions on the microscopy volume [12], or require post-hoc proofreading and editing of the reconstruction results [27, 3], each with task-specific assumptions that do not hold for densely labeled tracer projection volumes. As a result, most existing methods are not capable of generating large-scale, high-throughput and faithful streamlines from the tracer signal.

To bridge this gap, we propose ACMap (Fig. 1), a high-fidelity tracing method enabling fiber generation and direct integration of tracer and dMRI

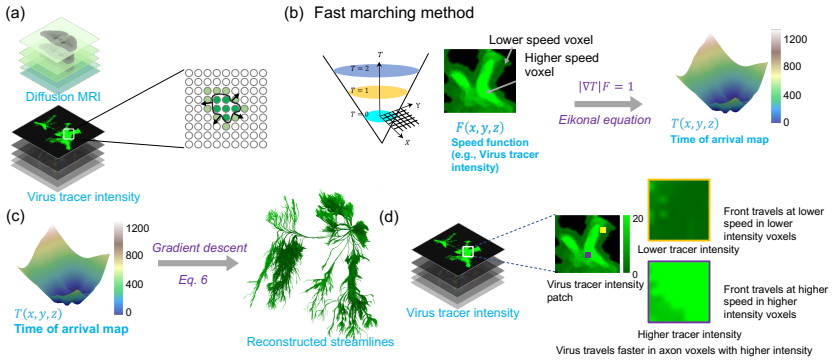


**Fig. 2. Generation of streamlines from primate virus tracer intensity using fast marching method.** (a) Leverage virus tracer intensity difference to generate advancing fronts; (b) Generation of time of arrival map from tracer intensity; (c) Generation of streamlines from time of arrival map; (d) Definition of speed function $F(x, y, z)$.

derived streamlines. ACMap is designed for the densely labeled and spatially smeared mesoscale tracer projections without assumptions about the fiber morphology. We exploit the virus tracing injection site to pose streamline reconstruction as a source-constrained shortest path problem. We then solve this problem by propagating wave fronts from the injection site and show that this process described by the Eikonal equation can be efficiently solved by the fast marching method (FMM) [17]. Experiments show that ACMap generates high-fidelity and dense streamlines, outperforming existing methods by a large margin. ACMap represents a significant step towards mapping across-scales connectivity of the brain, providing a new approach to validate and optimize dMRI tractography algorithms for accurate mapping of the brain-wide mesoscale connectome.

## 2 Method

### 2.1 General workflow of ACMap

As outlined in Fig. 2, to solve the streamline generation problem from virus tracing, we leverage virus tracer intensity difference to generate fronts (Fig. 2a) and time of arrival map by synergizing a simple and interpretable speed function (Fig. 2d) into the fast marching method (Fig. 2b), resulting in continuous tracking using gradient descent to generate high-fidelity fiber pathways (Fig. 2c).

### 2.2 Formulation of streamline generation problem from virus tracing

Virus tracing experiments provide a volumetric scalar measurement $I(\mathbf{x})$ that indicates the gold standard likelihood of axons, but does not directly provide per-voxel orientation. To address this, we treat streamline generation from virus

tracing as a shortest path optimization problem [18, 15], which can be seen as continuous front propagation from the injection site. We define the optimal pathways as the minimum cost trajectories connecting any spatial point $\mathbf{x} \in \Omega$ back to the injection site, denoted as $\mathcal{A}$. The cumulative traversal cost, or time of arrival map, $T(\mathbf{x})$ is defined as:

$$T(\mathbf{x}) = \min_{\gamma \in \Gamma} \int_0^L c(\gamma(\tau))\, d\tau \tag{1}$$

where $\Gamma$ is the set of all possible paths parameterized by arc length $\tau$, $L$ is the total length of the path, $\gamma(0) \in \mathcal{A}$, $\gamma(L) = \mathbf{x}$, and $c(\mathbf{x})$ represents the local cost for the front to cross location $\mathbf{x}$. Computing the global accumulative cost at each voxel given by Eq. 1 involves solving the Eikonal equation given below [18]:

$$|\nabla T(\mathbf{x})| F(\mathbf{x}) = 1, \quad T(\mathbf{x}) = 0 \text{ for } \mathbf{x} \in \mathcal{A} \tag{2}$$

where $F$ is the propagation speed and is related to the cost function by $F(\mathbf{x}) = \frac{1}{c(\mathbf{x})}$. In the following section, we first define the propagation speed $F(\mathbf{x})$ as an interpretable function of the observed tracer intensity $I(\mathbf{x})$. We then show that solving Eq. 2 using FMM yields an optimal time of arrival solution $T(\mathbf{x})$, from which continuous fiber pathways can be recovered by gradient descent [15, 18].

### 2.3 Generation of virus tracing streamlines using fast marching method (FMM)

**Definition of speed function in FMM** Since higher virus tracer intensity indicates higher likelihood of axon existence, we naturally assume that the front moves more quickly in high intensity regions, and more slowly in low intensity regions. Therefore, the speed function can be defined as:

$$F(\mathbf{x}) = I(\mathbf{x}) + \epsilon \tag{3}$$

where I(x) is tracer intensity, and $\epsilon$ is a small constant to help the tracking algorithm propagate through low intensity regions. Next we show how to calculate the first arrival time, i.e., minimum cost required for the front to traverse each tracer intensity voxel.

**Estimation of time of arrival map** FMM calculates the time-of-arrival field, $T(\mathbf{x})$, by partitioning the voxel grid into three dynamic sets: *frozen*, where arrival time is finalized, the *narrow band*, where voxels are currently being evaluated, and *unvisited*, where voxels are yet to be reached. To evaluate Eq. 2 at each voxel, the spatial gradient $|\nabla T(x)|$ is discretized using an upwind finite difference scheme:

$$\sum_{p \in \{x,y,z\}} \left(\max\{D_p^- T, -D_p^+ T, 0\}\right)^2 = \frac{1}{F^2} \tag{4}$$

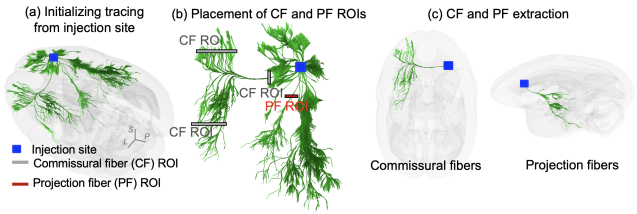


**Fig. 3. Commissural and projection fibers in the marmoset brain reconstructed by ACMap from virus tracing injected in a prefrontal cortex site.** (a) 3D surface view of all reconstructed fibers originating from the injection site; (b) "AND" ROI placement strategy for delineating the commissural (grey box) and projection (red box) fibers; (c) 3D surface view of the delineated commissural and projection fibers. Location of the injection site is indicated by blue box.

where $D_p^-$ and $D_p^+$ are the backward and forward difference operators, respectively. To improve sub-voxel accuracy, we use a higher accuracy second-order scheme to approximate these operators. For a given voxel at grid index $(i, j, k)$ with uniform grid spacing $h$, the operators for the $x$-dimension are defined as:

$$\begin{cases} D_x^- T_{i,j,k} = \frac{3T_{i,j,k} - 4T_{i-1,j,k} + T_{i-2,j,k}}{2h}, \\ D_x^+ T_{i,j,k} = -\frac{3T_{i,j,k} - 4T_{i+1,j,k} + T_{i+2,j,k}}{2h} \end{cases} \tag{5}$$

Note that when there are fewer than two upwind frozen neighbors for a voxel, e.g., the immediate neighbor voxels of the injection site, the approximation naturally falls back to first-order scheme. Substituting these spatial derivatives into Eq. 2 yields a quadratic equation in $T(\mathbf{x})$ and can be solved analytically.

**Continuous streamline tracking based on time of arrival maps** With the global minimum cost map $T$ established by the FMM, the optimal continuous streamlines can be traced back to the injection site by performing gradient descent following the negative gradient vector field of $T$ back to the injection site:

$$x_{t+1} = x_t - \alpha \frac{\nabla T}{|\nabla T|}, \qquad \text{given } x(0) = B, \tag{6}$$

where $\alpha$ is the step size and $B$ is the starting point of tracking. To mitigate tracking errors caused by acquisition and preprocessing noise, we integrate streamlines via fourth-order Runge-Kutta method, which samples the gradient at multiple sub-voxel intermediate points rather than relying on a single voxel estimate.

**Details of implementation** We use brute-force approach [5] in continuous tracking to avoid missing fibers caused by tracer intensity noise. The step size is set to 0.3 mm. The constant $\epsilon$ in Eq. 3 is set to 0.1. We use the multi-ROI (regions of interest) approach [22] for fiber delineation. Commissural fibers were delineated by filtering streamlines passing through two ROIs placed in two

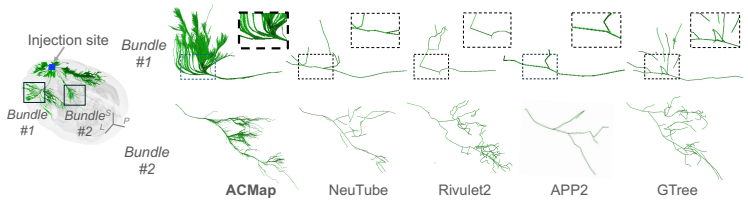


**Fig. 4. Qualitative comparison of streamlines derived from ACMap and other neuron tracing methods, including NeuTube, Rivulet2, APP2, GTree and D-LMBmap.** D-LMBmap result is not shown because no fiber can be traced with D-LMBmap.

coronal slices located in the anterior brain (Fig. 3), and projection fibers were delineated by placing an ROI in a middle coronal slice (Fig. 3). Probabilistic dMRI tractography with STTAR [26] protocol was applied on the multi-shell dMRI for reconstructing long-range fibers originating from the same ROI as the virus tracing injection site in the left prefrontal cortex. Fibers are visualized in DSIStudio [25].

## 3 Experiments and Results

**Dataset** We used paired preprocessed multi-shell dMRI and virus tracing data of the marmoset brain from the BMCR dataset [19]. It provides whole-brain anterograde tracer intensity volumes with a known injection site and long-range, densely distributed signal. Each pair of dMRI and tracer data is from the same brain. Virus tracer data of postmortem marmoset brain was acquired by placing anterograde TET-amplified AAV fluorescent neural tracer into the left hemisphere of the marmoset prefrontal cortex. Serial section images of the fluorescent anterograde tracer signals were acquired using serial two-photon tomography (STPT) with an in-plane resolution of $1.385 \times 1.399\ \mu m^2$, and slice thickness of $50\ \mu m$. Nissl and backlit sections were imaged with $3.774\ \mu m$/pixel. STPT image stitching was performed to stitch in-plane image tiles. Intensity correction was performed after stitching. 3D image stacks were produced by resampling the stitched images to $100\ \mu m$ isotropic. Virus tracer intensity data were rigorously processed for artifact mitigation by the original BMCR dataset providers [19], serving as the gold standard reference to evaluate traced streamlines across ACMap, competing streamline reconstruction methods and dMRI tractography. The injection site was delineated by the providers using a rigorous method to localize and detect labeled cell bodies with intensity above a certain threshold as the injection site [19]. The resolution of multi-shell dMRI of postmortem marmoset brain is isotropic 0.2 mm, acquired using a 2D spin echo EPI diffusion sequence on a Bruker 9.4T scanner. DMRI parameters were b =1000, 3000, 5000 $s/mm^2$, 128 unique gradient directions, TE = 28.4 ms, TR = 4s, for an imaging resolution of $0.2 \times 0.2 \times 0.2\ mm^3$. Details about dMRI preprocessing can be found in [19].

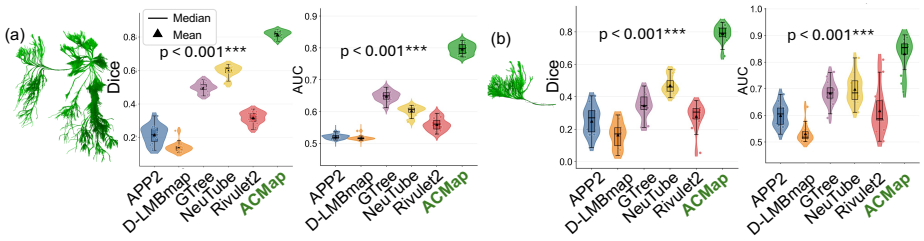


**Fig. 5. Quantitative comparison between ACMap and other neuron tracing methods for all fibers (a) and commissural fibers (b) from the injection site.** Other neuron tracing methods include NeuTube, Rivulet2, APP2, GTree and D-LMBmap. p<0.001*** after ANOVA test with FDR correction.

We evaluated ACMap on the BMCR [19] dataset with paired virus tracing and multi-shell dMRI data from the postmortem marmoset brain. We randomly selected 15 subjects as a test set. To further evaluate the reconstructed fiber morphology, we delineated the corpus callosum (CC) in the high intensity regions of the right hemisphere from the 15 subjects as an additional test set. CC was selected due to its distinguishable shape.

**Evaluation with other methods** We compared ACMap with several methods proposed in the neuron tracing field, including GTree [27], NeuTube [3], Rivulet2 [12] and APP2 [24]. We also compared with a learning-based dense axon segmentation method, D-LMBmap [10], to explore whether a direct segmentation could reconstruct the fine-grained fiber morphology. To evaluate the fidelity of streamlines, we used the area under the receiver operating characteristic (ROC) curve (AUC), and the Dice Similarity Coefficient as primary metrics. AUC measures how well the derived streamlines correctly distinguish high and low intensity voxels in the ground-truth tracer intensity and is threshold independent. We first converted streamlines to a density map that encodes the number of streamlines crossing each voxel. The AUC score was then calculated between the streamline density map and ground-truth tracer intensity. Dice score was calculated between binarized streamline density and tracer intensity. We followed a widely used binarization threshold of setting a voxel to 1 if traversed by at least one streamline and 0 otherwise [21] for Dice score evaluation, and applied this evaluation to ACMap and all competing methods.

**Comparison between ACMap and dMRI tractography** We computed the local streamline curvature $\kappa$ and compared the resulting curvature histograms to assess morphological consistency between ACMap-derived streamlines and dMRI tractography streamlines.

**Results** High-fidelity and dense long-range fibers are reconstructed by ACMap. The branching pattern of commissural fibers and distant projection fibers are

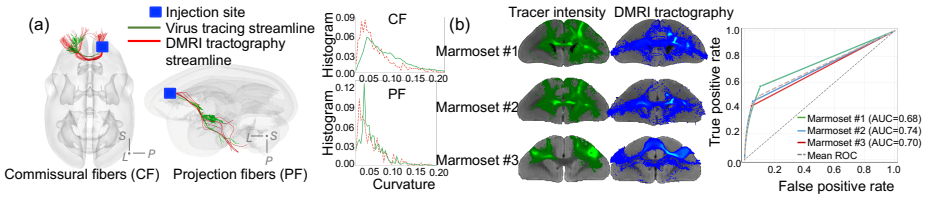


**Fig. 6. Application of high-fidelity ACMap for validating dMRI tractography.** (a) Axial and sagittal view of virus tracing-derived streamlines colored in green and dMRI tractography-derived streamlines colored in red originating from the same injection site. Highly overlapped histograms of streamline curvature from ACMap and dMRI tractography are also demonstrated on the right. (b) Reproducible validation of dMRI tractography with tracer intensity, demonstrated by ROC curves calculated from three marmoset brains.

well captured (Fig. 3). Compared to baseline neuron tracing methods, ACMap demonstrates a significant advantage in reconstructing dense, high-fidelity fiber trajectories (Fig. 4). While tracing methods like NeuTube [3] and GTree [27] can capture the primary fiber structures, they consistently failed to reconstruct the complex, fine-grained fiber branches, resulting in sparse and fragmented streamlines. Rivulet2 [12] and APP2 [24] exhibit severe under-tracing, missing substantial portions of the projection bundles entirely. D-LMBmap failed to trace continuous fibers in this application and its results are not shown.

The visual advantages of ACMap are supported by our quantitative evaluations. For the complete set of fibers originating from the injection site (Fig. 5), ACMap achieves the highest Dice and AUC scores, outperforming compared methods by a large margin. The high Dice and AUC scores of ACMap indicate that its high-fidelity streamlines accurately predict the ground-truth tracer intensity with high sensitivity. One-way ANOVA confirmed the comparison results were statistically significant ($p < 0.001$) after correcting for multiple comparisons with FDR.

Strong spatial correspondence was observed between the ACMap-derived virus tracing streamlines (green) and the dMRI tractography streamlines (red) originating from the same injection site, particularly along the commissural and projection fibers (Fig. 6a left and middle panel). The highly overlapped histograms of streamline curvature confirmed that the dMRI tractography derived by STTAR [26] reflects the true morphological curvature captured by ACMap (Fig. 6a right panel). Reproducible validation of dMRI tractography with tracer intensity was shown in Fig. 6b, demonstrated by ROC curves calculated from three marmoset brains.

## 4 Discussion and Conclusion

We developed ACMap, the first fast marching method for streamline generation based on virus tracing data on primate brains. ACMap seamlessly bridges multi-

modality imaging data with different resolutions and enables across-scales connectivity mapping. It can robustly and reproducibly generate high-fidelity and high-throughput long-range fibers from virus tracing, such as the demonstrated projection and commissural fibers, which are well aligned with histology-based marmoset atlas [16]. We demonstrated that ACMap outperforms other neuron tracing methods qualitatively in terms of generating continuous, dense streamlines and quantitatively in terms of truthfully reflecting the underlying tracer intensity map. ACMap also provides reliable gold standard streamlines for high-fidelity dMRI tractography validation. Understanding the limitation of limited injection site of adopted marmoset virus tracing dataset, future reproducibility studies conducting extensive and rigorous validation of ACMap with data from a large number of injection sites, across more primate brains and diverse datasets, e.g., [9], are warranted. Precise registration of injection site translated to fiber tractography initialization location is also critical for evaluating other fiber tracing methods. Future implementation of GPU acceleration will improve the computational efficiency of ACMap for more scalable reconstruction of whole-brain fiber pathways, and comprehensive runtime analysis will be included to evaluate the efficiency. By enabling direct integration of streamlines generated across scales, ACMap provides a novel and advanced framework for across-scales connectivity studies and validating the accuracy of dMRI-based tractography. It opens new avenues for developing tractography algorithms that can achieve accurate mapping of the brain-wide mesoscale connectome.

**Acknowledgments.** This study is funded by NIH R01MH092535, R01MH125333, R01EB031284, R01MH129981, R21MH123930 and P50HD105354.

**Disclosure of Interests.** The authors have no competing interests to declare that are relevant to the content of this article.

## References

1. Calabrese, E., Badea, A., Cofer, G., Qi, Y., Johnson, G.A.: A diffusion mri tractography connectome of the mouse brain and comparison with neuronal tracer data. Cerebral Cortex **25**(11), 4628–4637 (2015)
2. Feng, L., Jeon, T., Yu, Q., Ouyang, M., Peng, Q., Mishra, V., Pletikos, M., Sestan, N., Miller, M.I., Mori, S., et al.: Population-averaged macaque brain atlas with high-resolution ex vivo dti integrated into in vivo space. Brain Structure and Function **222**(9), 4131–4147 (2017)
3. Feng, L., Zhao, T., Kim, J.: Neutube 1.0: a new design for efficient neuron reconstruction software based on the swc format. Eneuro **2**(1) (2015)
4. Huang, H., Shu, N., Mishra, V., Jeon, T., Chalak, L., Wang, Z.J., Rollins, N., Gong, G., Cheng, H., Peng, Y., et al.: Development of human brain structural networks through infancy and childhood. Cerebral Cortex **25**(5), 1389–1404 (2015)
5. Huang, H., Zhang, J., Van Zijl, P.C., Mori, S.: Analysis of noise effects on dti-based tractography using the brute-force and multi-roi approach. Magnetic Resonance in Medicine: An Official Journal of the International Society for Magnetic Resonance in Medicine **52**(3), 559–565 (2004)

6. Huang, H., Zhang, J., Wakana, S., Zhang, W., Ren, T., Richards, L.J., Yarowsky, P., Donohue, P., Graham, E., van Zijl, P.C., et al.: White and gray matter development in human fetal, newborn and pediatric brains. Neuroimage **33**(1), 27–38 (2006)
7. Jbabdi, S., Lehman, J.F., Haber, S.N., Behrens, T.E.: Human and monkey ventral prefrontal fibers use the same organizational principles to reach their targets: tracing versus tractography. Journal of Neuroscience **33**(7), 3190–3201 (2013)
8. Kaur, N., Kovner, R., Gulden, F.O., Pletikos, M., Andrijevic, D., Zhu, T., Silbereis, J., Shibata, M., Shibata, A., Liu, Y., et al.: Specification of claustro-amygdalar and palaeocortical neurons and circuits. Nature **638**(8050), 469–478 (2025)
9. Kuan, L., Li, Y., Lau, C., Feng, D., Bernard, A., Sunkin, S.M., Zeng, H., Dang, C., Hawrylycz, M., Ng, L.: Neuroinformatics of the allen mouse brain connectivity atlas. Methods **73**, 4–17 (2015)
10. Li, Z., Shang, Z., Liu, J., Zhen, H., Zhu, E., Zhong, S., Sturgess, R.N., Zhou, Y., Hu, X., Zhao, X., et al.: D-lmbmap: a fully automated deep-learning pipeline for whole-brain profiling of neural circuitry. Nature Methods **20**(10), 1593–1604 (2023)
11. Liang, Z., Arefin, T.M., Lee, C.H., Zhang, J.: Using mesoscopic tract-tracing data to guide the estimation of fiber orientation distributions in the mouse brain from diffusion mri. Neuroimage **270**, 119999 (2023)
12. Liu, S., Zhang, D., Song, Y., Peng, H., Cai, W.: Automated 3-d neuron tracing with precise branch erasing and confidence controlled back tracking. IEEE Transactions on Medical Imaging **37**(11), 2441–2452 (2018)
13. Maffei, C., Girard, G., Schilling, K.G., Aydogan, D.B., Adluru, N., Zhylka, A., Wu, Y., Mancini, M., Hamamci, A., Sarica, A., et al.: Insights from the irontract challenge: Optimal methods for mapping brain pathways from multi-shell diffusion mri. NeuroImage **257**, 119327 (2022)
14. Ouyang, A., Jeon, T., Sunkin, S.M., Pletikos, M., Sedmak, G., Sestan, N., Lein, E.S., Huang, H.: Spatial mapping of structural and connectional imaging data for the developing human brain with diffusion tensor imaging. Methods **73**, 27–37 (2015)
15. Parker, G.J., Wheeler-Kingshott, C.A., Barker, G.J.: Estimating distributed anatomical connectivity using fast marching methods and diffusion tensor imaging. IEEE Transactions on Medical Imaging **21**(5), 505–512 (2002)
16. Paxinos, G., Rosa, M., Merlin, S., Majka, P.: The marmoset brain in stereotaxic coordinates. Academic Press (2025)
17. Sethian, J.A.: A fast marching level set method for monotonically advancing fronts. Proceedings of the National Academy of Sciences **93**(4), 1591–1595 (1996)
18. Sethian, J.A., et al.: Level set methods and fast marching methods, vol. 98. Cambridge Cambridge UP (1999)
19. Skibbe, H., Rachmadi, M.F., Nakae, K., Gutierrez, C.E., Hata, J., Tsukada, H., Poon, C., Schlachter, M., Doya, K., Majka, P., et al.: The brain/minds marmoset connectivity resource: An open-access platform for cellular-level tracing and tractography in the primate brain. PLoS Biology **21**(6), e3002158 (2023)
20. Skibbe, H., Reisert, M., Nakae, K., Watakabe, A., Hata, J., Mizukami, H., Okano, H., Yamamori, T., Ishii, S.: Pat—probabilistic axon tracking for densely labeled neurons in large 3-d micrographs. IEEE Transactions on Medical Imaging **38**(1), 69–78 (2018)
21. Wakana, S., Caprihan, A., Panzenboeck, M.M., Fallon, J.H., Perry, M., Gollub, R.L., Hua, K., Zhang, J., Jiang, H., Dubey, P., Blitz, A., van Zijl, P., Mori, S.: Reproducibility of quantitative tractography methods applied to cerebral white matter. NeuroImage **36**(3), 630–644 (2007)

22. Wakana, S., Jiang, H., Nagae-Poetscher, L.M., Van Zijl, P.C., Mori, S.: Fiber tract–based atlas of human white matter anatomy. Radiology **230**(1), 77–87 (2004)
23. Wang, Q., Ding, S.L., Li, Y., Royall, J., Feng, D., Lesnar, P., Graddis, N., Naeemi, M., Facer, B., Ho, A., et al.: The allen mouse brain common coordinate framework: a 3d reference atlas. Cell **181**(4), 936–953 (2020)
24. Xiao, H., Peng, H.: App2: automatic tracing of 3d neuron morphology based on hierarchical pruning of a gray-weighted image distance-tree. Bioinformatics **29**(11), 1448–1454 (2013)
25. Yeh, F.C.: Dsi studio: an integrated tractography platform and fiber data hub for accelerating brain research. Nature Methods **22**(8), 1617–1619 (2025)
26. Zhao, C., Ouyang, M., Yu, Q., Huang, H.: Short-range tractography with high throughput and reproducibility (sttar) characterized by fdt tracing and hdbscan clustering. In: Proceedings of ISMRM. vol. 857 (2020)
27. Zhou, H., Li, S., Li, A., Huang, Q., Xiong, F., Li, N., Han, J., Kang, H., Chen, Y., Li, Y., et al.: Gtree: an open-source tool for dense reconstruction of brain-wide neuronal population. Neuroinformatics **19**(2), 305–317 (2021)